Eur. J. Mineral., 34, 493–506, 2022
https://doi.org/10.5194/ejm-34-493-2022

European Journal of Mineralogy
Open Access

Weathering of stannite–kësterite [$Cu_2(Fe,Zn)SnS_4$] and the environmental mobility of the released elements

Patrick Haase[1], **Stefan Kiefer**[1], **Kilian Pollok**[1], **Petr Drahota**[2], **and Juraj Majzlan**[1]

[1]Institute of Geosciences, Friedrich Schiller University, Jena, Germany
[2]Institute of Geochemistry, Mineralogy and Mineral Resources, Charles University, Prague, Czech Republic

Correspondence: Patrick Haase (patrick.haase@uni-jena.de)

Received: 12 July 2022 – Revised: 12 September 2022 – Accepted: 24 September 2022 – Published: 21 October 2022

Abstract. The sulfidic waste dumps of the historical mining sites Giftkies and Kaňk (Czech Republic) have been exposed to a temperate climate over decades. This exposure generated low-pH conditions caused by metal sulfide decomposition. Tin sulfides of the stannite–kësterite series [$Cu_2(Fe,Zn)SnS_4$] are common Sn minerals in the ores at the investigated sites. They decompose under acidic and oxidizing conditions and form in situ secondary precipitates. Compositional analyses of primary and secondary minerals were collected by electron microprobe to track the environmental mobility of the released elements during weathering. Transmission electron microscopy revealed a diffusion-driven alteration of stannite to Sn-rich chalcopyrite and the precipitation of native copper and silver from stannite. In assemblages containing arsenopyrite, an in situ and amorphous Sn–Fe–As (SFA)-rich phase precipitated close to the Sn sulfide. The SFA precipitate contains very little sulfur, which was probably released to the aqueous phase as oxidized species, whereas small amounts of Cu and Zn were captured by the SFA. This precipitate is metastable and acts as a temporaneous sink for mobile elements (Cu, Zn) and elements derived from acid-soluble silicates and phosphates (Ca, Si, Al, and P). With advanced weathering, complex redox reactions result in the precipitation of magnetite as an oxidation product of the sulfidic material under oxidative conditions. The stable minerals goethite and cassiterite mark the end of the weathering sequence and crystallized from the amorphous SFA precipitate.

1 Introduction

In nature, primary tin deposits are often associated with hydrothermal systems linked to granite intrusions. Micas, especially muscovite (Neiva, 1984; Smeds, 1992), and Fe- and Ti-bearing minerals (e.g. hornblende, titanite; Eugster, 1984; Chen et al., 2022) are the most important Sn carriers during cooling and crystallization of the granitic melts. It was assumed that Sn^{4+} substitutes in the rock-forming minerals (e.g. biotite) for Ti^{4+} or Fe^{3+} (Eugster, 1984; Smeds, 1992; Chen et al., 2022). The tin remobilization from these minerals highly depends on the chlorinity of the hydrothermal fluids, in order to form Sn chloro-complexes (Eugster, 1984; Müller, 1999; Schmidt, 2018). Changing fluid conditions results in the precipitation of Sn minerals in hydrothermal systems, especially cassiterite (SnO_2) or sulfides of the stannite–kësterite series (Cu_2BSnS_4, $B = Fe^{2+}$, Zn; Springer, 1968). Other Sn-containing sulfides are chalcopyrite ($CuFeS_2$) and sphalerite (ZnS) with amounts up to 2.4 wt % (Kase, 1987; Gena et al., 2005) and up to 0.57 wt % Sn (Dobrovol'skaya et al., 2008), respectively. Both nominally Sn-free minerals often occur in aggregates with stannite–kësterite in Sn deposits (Landes, 1928). Cassiterite was shown to be stable over a large pH range (Rai et al., 2011). Leachates generated by the natural runoff from tailings contain < 0.01 mg L^{-1} Sn where cassiterite is the solubility-controlling phase for Sn (Lottermoser and Ashley, 2006; Romero et al., 2014). Weathering of the stannite–kësterite sulfides results in the formation of cassiterite (Coleman, 1953; Karwowski and Włodyka, 1981). Previous studies have indicated the formation of heterogeneous precipitates consisting of "cassiterite and an unidentified mineral of Cu" (Černý et al., 2001), "cuprocassiterite" (Landes, 1928), mushistonite (Durant and Parkinson, 2016), or "colloform mixtures of hydroxides rich in tin" (Karwowski and Włodyka, 1981). The decomposi-

tion of the primary tin-bearing sulfides could be driven by hydrothermal alteration or exhumation followed by subsequent weathering under near-surface conditions. Our incomplete knowledge of the decomposition of Sn sulfides may lead to incorrect assumptions and predictions concerning the release of tin to or immobilization of tin in the environment. Other elements (e.g. Fe, As) released from the weathering of stannite–kësterite and accompanying sulfides (e.g. arsenopyrite) may also interact with tin and could influence its environmental mobility and vice versa. Both arsenic and Fe are common elements in hydrothermal systems and are incorporated in arsenopyrite (FeAsS) or arsenian pyrite ($Fe(S,As)_2$) (Abraitis et al., 2004). Both are well investigated and abundant minerals in most Sn ore deposits and decompose under near-surface conditions. Their decomposition leads to the release of arsenic and the formation of iron oxyhydroxide coatings (Drahota and Filippi, 2009), iron sulfates, or iron arsenate rims depending on prevailing conditions (Thornber, 1985; Chandra and Gerson, 2010; Courtin-Nomade et al., 2010). These in situ secondary precipitates immobilize elements from solution and partly retard further decomposition of the primary mineral (Jambor and Dutrizac, 1998). They also document the environmental mobility of elements and can provide further information about the destination of Sn.

In this work, we collected dump material from two sites where Sn sulfides have been exposed to ambient conditions for decades. The chemical composition of the ore minerals and secondary products were analysed by electron microprobe (EMP). Focused ion beam scanning electron microscopy (FIB–SEM) and transmission electron microscopy (TEM) were used to examine selected areas containing primary Sn sulfides and secondary precipitates to track the fate of tin. The results shall improve our comprehension of the transfer of tin from primary minerals to secondary products and the complex interaction of Sn with other elements.

2 Material and methods

Samples were collected from uncovered dumps of the adit Giftkies (50°23′38.6″ N, 12°55′57.3″ E) close to Jáchymov and Kaňk (49°58′14.7″ N, 15°16′18.8″ E) near Kutná Hora, both located in the Czech Republic. At Giftkies, the mica schist rocks were greisenized by a granitic intrusion of Variscan age followed by several hydrothermal fluid events rich in Ag–As–Bi–Co–Ni–U (Filippi et al., 2015; Ondruš et al., 2003). This led to a complex assemblage of ore minerals with the most abundant sulfide arsenopyrite at this site, whereas chalcopyrite, pyrite, and Sn sulfides of the stannite–kësterite series are less common (Filippi et al., 2015). The As minerals were mined in three adits from the 17th to the 18th century, and their waste dumps have remained uncovered since this time (Kořan and Mrňa, 1967, in Filippi et al., 2015). Kaňk is part of the Kutná Hora ore district situated in the northern part of the Moldanubian Zone. The host rocks are biotite gneiss and migmatites. Plutonic intrusions generated fissures in the host rock in the Variscan age and were later mineralized during several hydrothermal stages (Ettler et al., 2010). Over 10 active Ag mines and their associated overburdens are known in this area from the 15th to the 16th century (Kocourková-Víšková et al., 2015). The large waste dumps have remained since this time and contain the ore minerals arsenopyrite and less common pyrite, sphalerite, galena, pyrrhotite, and scarce stannite (Kocourková-Víšková et al., 2015). The collected material was sieved in the field to obtain the fraction < 2.5 mm to remove coarse biogenic material (e.g. roots) and achieve representative samples. The heavy mineral fractions from each location were further separated from the light fraction ($< 2.8\,g\,cm^{-2}$). Each fraction was finally prepared as a standard polished section.

The ore minerals and secondary precipitates were investigated for major and minor elements by electron microprobe (EMP) using a JEOL JXA-8230 instrument. Initial screening was done by energy-dispersive X-ray (EDX) analyses to check which elements are present. The measurement conditions of wavelength-dispersive X-ray (WDX) analyses for the sulfides were set to an accelerating voltage of 20 kV, a beam current of 20 nA, and a beam diameter of 1 µm. WDX was used to measure the X-ray lines of the elements S ($K\alpha$), Fe ($K\alpha$), Cu ($K\alpha$), Zn ($K\alpha$), As ($K\alpha$), Ag ($L\alpha$), Cd ($L\alpha$), and Sn ($L\alpha$). Counting times were set to 40 s to improve the count rate. The standards used for calibration were pyrite for S and Fe, chalcopyrite for Cu, sphalerite for Zn, arsenopyrite and InAs for As, elemental Ag for Ag, CdS for Cd, and cassiterite for Sn. The detection limits were calculated from the background counts, the measurement time, and the standard material concentration. They are 0.02 wt % for S, 0.03 wt %–0.04 wt % for Fe, 0.04 wt %–0.05 wt % for Cu, 0.04 wt %–0.05 wt % for Zn, 0.07 wt %–0.09 wt % for As, 0.04 wt % for Ag, 0.07 wt % for Cd, and 0.03 wt % for Sn. Secondary products, especially poorly crystalline phases, are more sensitive to a high accelerating voltage and beam current. Therefore, the focused beam settings were reduced to 15 kV and 15 nA. The measured elements and their X-ray lines were Si ($K\alpha$), P ($K\alpha$), S ($K\alpha$), Ca ($K\alpha$), Fe ($K\alpha$), Cu ($K\alpha$), Zn ($K\alpha$), As ($K\alpha$), Ag ($L\alpha$), Cd ($L\alpha$), Sn ($L\alpha$), and Pb ($M\alpha$) at counting times of 40 s. The standards used for the oxidized phases were orthoclase for Si, apatite for P, baryte for S, wollastonite for Ca, hematite for Fe, chalcopyrite for Cu, sphalerite for Zn, arsenopyrite and InAs for As, elemental Ag for Ag, cassiterite for Sn, galena for Pb, and elemental Bi for Bi. The detection limits for the oxide measurements were calculated in the same way as mentioned above and amount to 0.03 wt %–0.04 wt % for Si, 0.04 wt % for P, 0.03 wt %–0.05 wt % for S, 0.03 wt % for Ca, 0.04 wt % for Fe, 0.05 wt %–0.07 wt % for Cu, 0.04 wt %–0.05 wt % for Zn, 0.07 wt %–0.11 wt % for As, 0.04 wt %–0.07 wt % for Ag, 0.03 wt %–0.05 wt % for Sn, 0.08 wt %–0.11 wt % for Pb, and 0.07 wt % for Bi. Overlap corrections were performed for the peaks of Sn / Cd, Fe / Pb, As / Pb, Ca / Sn, and As / Sn.

An SEM FEI Quanta 3D FEG was used for focused ion beam preparation of selected areas for subsequent TEM analysis. At first, a platinum lamella with a thickness of 3 µm was deposited on the surface of the area of interest. This protected the sample from the following ionization step where two trenches were cut with metallic gallium with a depth of 15 µm at a current of 15 nA. The slice was then cleaned and thinned on both sides at 3 nA and lowering to the end with 1 nA to receive a thickness of less than 1 µm. The lamella was then transferred to a FIB copper grid using an OmniProbe micromanipulator and finally thinned to about 100 nm using ion currents down to 100 pA. TEM was performed with an FEI Tecnai G2 FEG operated at 200 kV equipped with an X-Max^n 80T SDD EDX system (Oxford Instruments), a HAADF STEM detector (Fischione), and two 2K CCD Gatan cameras.

3 Results

3.1 Primary sulfides

Primary Sn sulfides are common in the heavy mineral fraction and belong to the stannite–kësterite series. They are anhedral and always show corroded edges (Fig. 1a–c). The chemical analyses show variations among the individual grains (Fig. 2, Table S1), and representative data are shown in Table 1. A few grains from Kaňk are extremely Fe-rich and Sn-poor, containing up to 28.55 wt % Fe and only 2.83 wt %–7.73 wt % Sn (Table S1), and belong to Sn-rich chalcopyrite (chalcopyrite I). In addition to the main elements in stannite and kësterite (Fig. 2), Cd, As, and Ag were also detected as minor elements. Cobalt, Ni, Bi, and Sb were not detected (Table S1). The analyses (excluding the Sn-rich chalcopyrite) were used to calculate the chemical formulae based on 4 S atoms per formula unit (apfu). Cadmium was assumed to substitute for the divalent cations in the position *B*, as in the Cd-endmember černýite (Cu_2CdSnS_4; Kissin et al., 1978). The černýite component in stannite–kësterite from both localities does not exceed 10 mol %. Silver substitutes for Cu as the Ag endmembers hocartite (Ag_2FeSnS_4; Caye et al., 1968) and pirquitasite (Ag_2ZnSnS_4; Johan and Picot, 1982) depending on the occupation of the *B* site. The Ag component is not higher than 5 mol % for stannite–kësterite from Kaňk. The average chemical formula for the stannite–kësterite series from Giftkies is $Cu_{1.98}(Fe_{0.70}Zn_{0.32}Cd_{0.01})_{\Sigma 1.03}As_{0.02}Sn_{0.93}S_4$ from 157 analyses in 59 grains, and that for Kaňk is $(Cu_{1.89}Ag_{0.01})_{\Sigma 1.90}(Fe_{0.89}Zn_{0.20})_{\Sigma 1.09}As_{0.01}Sn_{0.93}S_4$ from 88 analyses in 34 grains.

Several grains show a variation in Fe and Zn of up to 0.2 apfu. The molar $[Fe^{2+}/(Fe^{2+}+Zn)]$ ratio of all stannite–kësterite ranges from 0.30 mol % to 0.98 mol % and 0.64 mol % to 0.95 mol % at Giftkies and Kaňk, respectively (Table S1). An Fe–Zn plot illustrates the compositional range between the endmember stannite and kësterite (Fig. 3). Most of the analyses show excess [Fe + Zn] with respect to the nominal formulae (Table 1).

The most common sulfide in the sections from Giftkies and Kaňk is arsenopyrite. Pyrite is rare and was only found in samples from Kaňk. Arsenopyrite and pyrite always show corroded edges or occur as relics enclosed by their weathering products (Fig. 1d, e). WDX analyses of arsenopyrite show no incorporation of non-stoichiometric elements, whereas pyrite contains small amounts of As (Table 2). A second type of chalcopyrite (chalcopyrite II) with low abundance is found as anhedral grains influenced by weathering (Fig. 1f). They are not associated with stannite and contain only small amounts of Sn up to 0.7 wt % (Table S2) with an average of 0.23 wt % Sn and 0.15 wt % Sn for Giftkies and Kaňk, respectively (Table 2).

3.2 Cassiterite

Cassiterite from Giftkies and Kaňk is euhedral to subhedral. At Giftkies, more than 70 analyses gave an average composition of 97.85 wt % SnO_2, 0.75 wt % TiO_2, 0.49 wt % Fe_2O_3, 0.30 wt % WO_3, 0.27 wt % V_2O_3, and 0.12 wt % SiO_2. At Kaňk, cassiterite contains 99.78 wt % SnO_2, 1.06 wt % Fe_2O_3, and 0.20 wt % CaO averaged from 16 analyses at 7 different grain spots. Other analysed elements occur in traces (< 0.1 wt %).

3.3 Amorphous secondary precipitates

The secondary precipitates of Giftkies and Kaňk often occur within cracks and as rims encapsulating primary sulfides (Fig. 1). As the weathering advances, the secondary products may completely replace the primary sulfide grains. The secondary products are porous, fine-grained, and presumably contain volatile components (most likely H_2O). This assumption is in agreement with EMP analytical sums of 56 wt %–100 wt % (Table S3). The secondary precipitates can be divided into amorphous Sn–Fe–As (SFA)-rich phases, ferric arsenates (AFAs), and hydrous ferric oxides (HFOs) occurring at both locations.

The weathering products of stannite–kësterite form thick rims on the primary sulfides and belong to the amorphous SFA phases. At Giftkies, they are depleted in Zn, Cu, and S compared to the primary parent sulfides (Fig. 4). At Kaňk, these oxide components partially remained within the rims with up to 10.81 mol % CuO and 5.17 mol % ZnO. Other oxide components, such as Fe_2O_3 and SnO_2, occur and may even be enriched within the secondary precipitates compared to the Sn sulfides at both locations. Only a few WDX analyses indicate low Sn and high Fe in some grains (Fig. 5) found at the margins of Sn-rich chalcopyrite. Overall, the secondary Sn precipitates are mainly composed of $SnO_2 > Fe_2O_3 \approx As_2O_5$ (all in mol %; Fig. 4). These three components make up 39 mol %–97 mol % of the total oxide

Table 1. Ideal composition of members of the stannite–kësterite series and representative EMP analyses from stannite–kësterite of Giftkies and Kaňk. Values are given in percent by weight (wt %).

	Stannite Cu_2FeSnS_4	Ferrokësterite $Cu_2(Fe_{0.25}Zn_{0.75})SnS_4$	Kësterite Cu_2ZnSnS_4	1	2	3	4	5
Cu	29.56	29.08	28.92	30.62	27.63	31.28	28.11	28.03
Fe^{2+}	12.99	3.19	–	12.87	7.37	9.32	11.77	11.60
Zn	–	11.22	14.88	0.53	8.30	3.47	4.19	3.51
Sn	27.61	27.16	27.01	26.29	25.94	25.92	25.99	25.85
S	29.83	29.34	29.19	29.57	30.09	29.85	30.42	30.28
Σ	100	100	100	99.87	99.33	99.84	100.47	99.27

1: Giftkies GII06_05_01; 2: Giftkies H5_28a_02; 3: Kaňk KH5_05a_01_02; 4: Kaňk KH6_02_ 02_02; 5: Kaňk KH6_05_02_03.

Table 2. Mean values of EMP analyses of nominally Sn-free sulfides of Giftkies and Kaňk (apy, arsenopyrite; cp II, chalcopyrite II; py, pyrite). Values are given in percent by weight (wt %). All analyses are listed in Table S2.

	Giftkies		Kaňk		
	Apy ($n = 42$)	Cp II ($n = 17$)	Apy ($n = 23$)	Cp II ($n = 6$)	Py ($n = 10$)
As	48.70	0.03	43.80	0.12	0.14
Cu	0.01	35.02	0.04	33.94	0.01
Fe	33.85	29.46	34.99	29.65	45.89
S	18.42	34.02	21.13	35.40	54.63
Sn	< 0.01	0.23	0.01	0.15	< 0.01
Zn	0.01	0.04	0.05	0.16	0.01
Σ	101.07	98.85	100.07	99.51	100.70

mole percent. SFA also contains significant amounts of SiO_2 at Kaňk (Fig. 4).

Arsenopyrite weathering results in the formation of in situ As- and Fe-rich precipitates referred to as AFA. They are depleted in S compared to the primary sulfide. More than 70 analyses gave an overall compositional range of 17.1 mol %–51.2 mol % As_2O_5 and 37.2 mol %–67.0 mol % Fe_2O_3 (Fig. 5). They also contain small amounts of other oxides in variable amounts. At Giftkies, the averages of the minor oxides (> 0.2 mol %) are 0.43 mol % Al_2O_3, 1.43 mol % PbO, 0.27 mol % SiO_2, 2.85 mol % SO_3, 2.43 mol % CaO, 0.73 mol % CuO, and 1.01 mol % P_2O_5. At Kaňk, the precipitates contain 0.45 mol % Al_2O_3, 0.18 mol % PbO, 2.81 mol % SiO_2, 1.15 mol % SO_3, 14.96 mol % CaO, 1.45 mol % CuO, and 5.82 mol % ZnO.

Other Fe-rich secondary precipitates are ferric oxides not associated with arsenopyrite. They are summarized and referred to here as hydrous ferric oxides (HFOs) even if there are few compositions which are almost free of volatiles. They were formed especially from pyrite and to a lesser extent from chalcopyrite. Pyrite and chalcopyrite are rare and show thick weathering rims (Fig. 1d, f) indicating enhanced weathering. In most cases, HFOs coat silicates and oxides. Less common are pseudomorphs of HFOs after primary sulfides. WDX analyses of 58 spots on HFOs from Giftkies and Kaňk showed a compositional range from 64.3 mol %–99.4 mol % Fe_2O_3, with up to 19.4 mol % As_2O_5 and 0.55 mol % SnO_2 (Fig. 5).

3.4 TEM of Sn sulfide weathering zones

A lamella was prepared by FIB from weathered stannite of the location Kaňk (Fig. 6a). A representative profile between points X and Y suggests the occurrence along this X–Y profile of an almost symmetric sequence of stannite–Sn-rich chalcopyrite–native copper–SFA–(magnetite)–goethite–cassiterite from the rims towards the centre of the lamella.

Stannite occurs only at point Y at the bottom of the lamella in Fig. 6a and is homogenous, compact, and unweathered. Before cutting out the lamella, several EMP analyses were performed in the stannite and are shown in Fig. 1b (Table 3), and they showed a similar composition throughout the whole grain. The structure of stannite was confirmed by selected-area electron diffraction (SAED) (Fig. 6b). It has a distinct contact boundary with a compact and heterogenous Sn-rich chalcopyrite (close to point Y). EMP–WDX analyses were performed on a similar Sn-rich chalcopyrite at point X in Fig. 6a and support the presence of chalcopyrite instead of stannite because of the low Sn content (Table 3). However, there are local enrichments of Zn (Fig. 6a) and concomitant depletions of Fe and Cu in this chalcopyrite (Fig. 7) as shown by EDX analyses. These zinc-rich patches occur within this chalcopyrite without causing modifications of the structure,

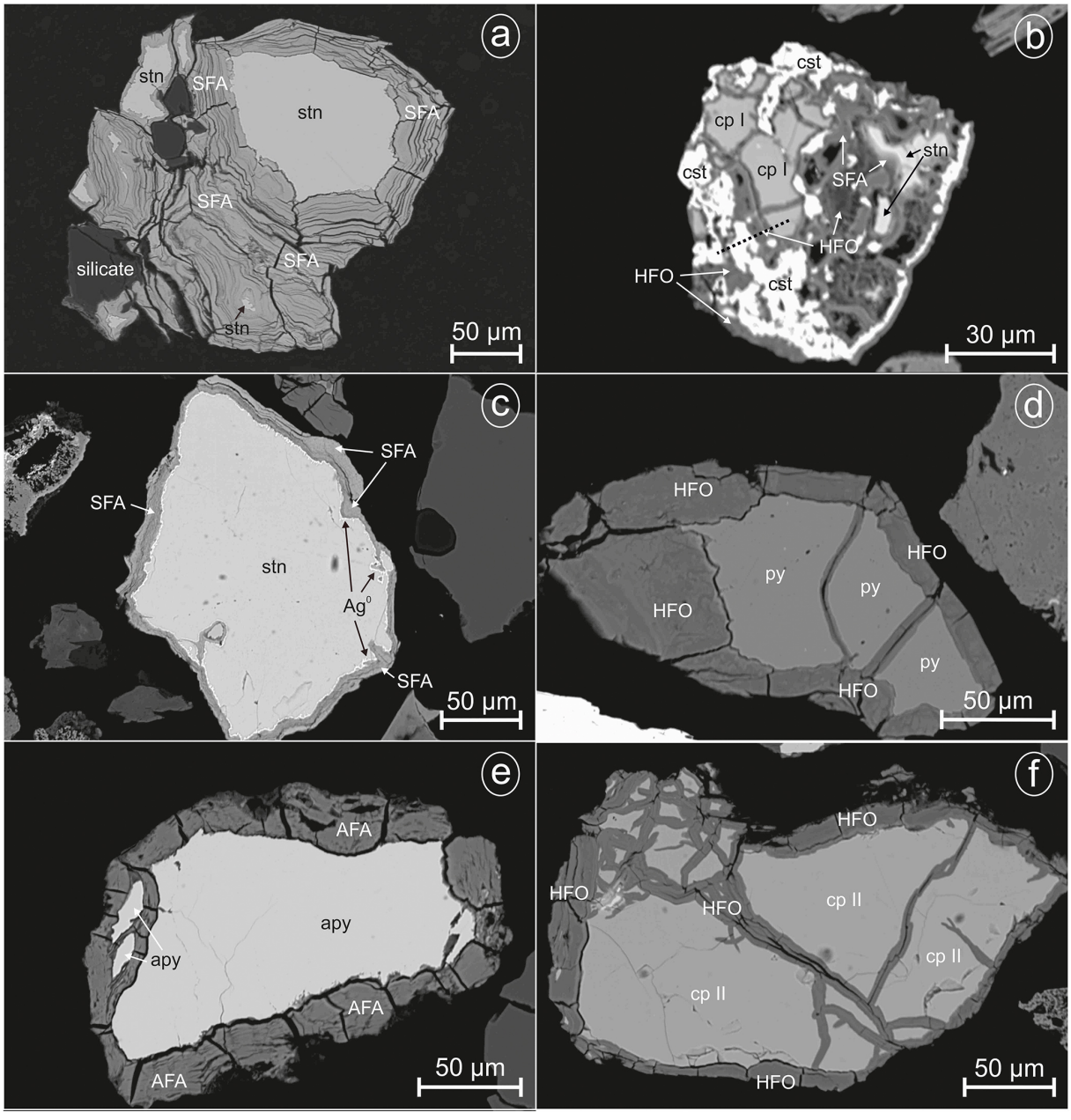

Figure 1. EMP images of investigated sulfides from Giftkies and Kaňk: **(a)** stannite with extensive weathering rim, **(b)** grain with stannite and its weathering products (dashed black line marks the TEM section in Fig. 6), **(c)** weathered stannite with a small cover of elemental silver, **(d)** relict of pyrite replaced by HFO, **(e)** weathered arsenopyrite replaced by AFA, and **(f)** chalcopyrite remnant with replacements of HFO; (AFA, amorphous ferric arsenate; Ag^0, native silver; apy, arsenopyrite; cp I, Sn-rich chalcopyrite (chalcopyrite I); cp II, chalcopyrite II; cst, cassiterite; HFO, hydrous ferric oxide; py, pyrite; SFA, amorphous Sn–Fe–As phase; stn, stannite).

as confirmed by SAED (Fig. 6c). Weaker spots at the half distance between the strongest reflections in the electron diffraction pattern indicate a superstructure in the Sn-rich chalcopyrite. Furthermore, chalcopyrite contains small sphalerite inclusions as shown by TEM–EDX and electron diffraction.

The secondary products of the Sn sulfide weathering are in situ precipitates. Native copper formed polycrystalline aggregates at the outer rims and in thin fractures of stannite as shown by TEM–EDX and electron diffraction. An amorphous and porous SFA precipitate coats the Sn sulfides and native copper. The SFA precipitate is enriched in Fe and depleted in Cu, Zn, Sn, and S compared to stannite (Table 3). Arsenic is not abundant in this SFA but shows a small enrichment compared to the primary Sn sulfides, and its distribution is heterogenous (Fig. 7). SAED patterns showed only

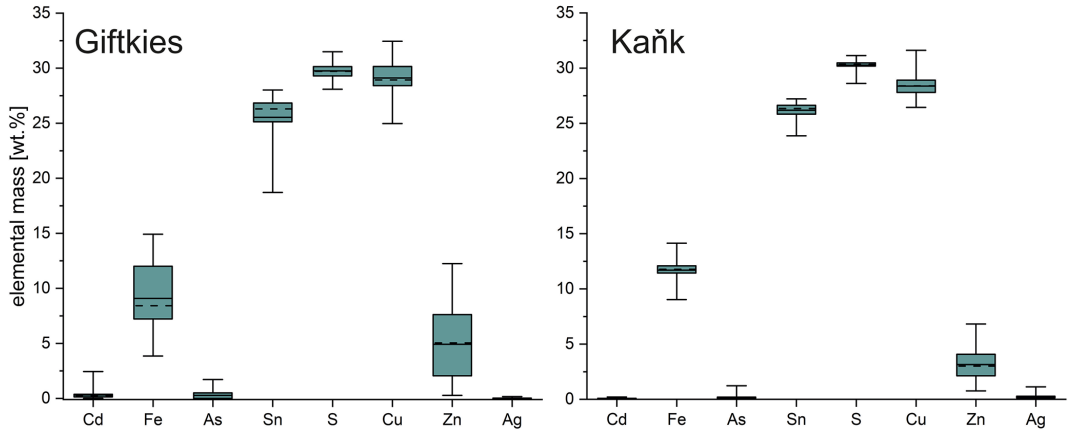

Figure 2. Box plot of the compositional range of stannite from Giftkies ($n = 157$) and Kaňk ($n = 88$) (average: solid line; median: dashed line; box: 25th–75th percentile; range: minimum–maximum (includes outliers)).

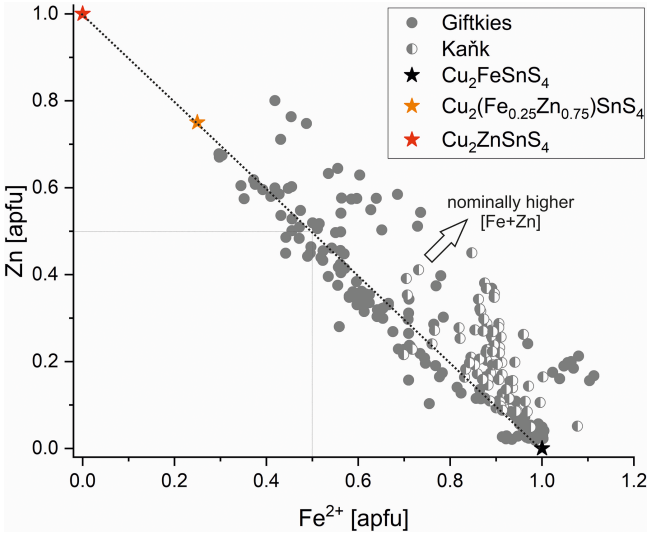

Figure 3. Calculated Fe^{2+} and Zn (apfu) based on 4 S atoms of the stannite–kësterite series from Giftkies and Kaňk and nominal compositions of the endmembers.

two broad rims (Fig. 6d), confirming the amorphous nature of this phase.

Further secondary products are magnetite (or maghemite), goethite, and cassiterite, which are not in direct contact with the Sn sulfides. Magnetite ($Fe^{2+}Fe^{3+}O_4$) and maghemite (γ-$Fe_2^{3+}O_3$) are chemically and structurally closely related. The identification as magnetite (rather than maghemite) is supported by the calculation of the Fe / O ratio after performing absorption corrections and normalization of the TEM–EDX analyses. Magnetite crystals are adjacent to the amorphous SFA precipitate and possess acicular morphology, which is unusual for this mineral. The electron diffraction pattern is consistent with the spinel structure with a dynamically stimulated reflection pair at $d_{200} = 4.20$ Å (derived from $d_{400} =$ 2.10 Å, Fig. 6e). Further reflections with a lower intensity in Fig. 6e are caused by co-stimulated goethite. Goethite occurs as a porous mass with low crystallinity. TEM–EDX analyses of goethite showed a lower calculated Fe / O ratio than that of magnetite and up to 3 wt % As. The structure of the polycrystalline aggregates of goethite was confirmed by electron diffraction (Fig. 6f).

Cassiterite is euhedral to subhedral and is adjacent to magnetite, goethite, and the SFA precipitate. WDX analyses gave an almost pure nominal composition with only small amounts of iron (Table 3). Its structure was confirmed by SAED (Fig. 6g).

Another TEM lamella from Giftkies contained a homogenous primary single crystal of stannite (Fig. 8a) with composition $Cu_{1.92}(Fe_{0.65}Zn_{0.30}Cd_{0.01})_{\Sigma 0.95}As_{0.06}Sn_{0.98}S_4$ (calculated from WDX analyses in Table 4). The structure is confirmed by electron diffraction (Fig. 8b).

The adjacent porous and homogenous secondary precipitate is amorphous (Fig. 8c). Several WDX analyses were performed in the broad SFA rim. The SFA precipitate is enriched in SnO_2 and to a lesser extent in Fe_2O_3 and As_2O_5 compared to stannite (Table 4). Copper, Zn, and S are almost lost.

Native silver occurs close to the stannite surface, proven by EMP and TEM. WDX analysis performed in SFA close to the stannite gave up to 10 wt % AgO (Table 4). TEM–EDX and electron diffraction identified native silver (Fig. 8d) and copper particles at and close to the reacting interface in thin fractures of the SFA phase. The occurrence of native metals instead of oxides in SFA results in the higher apparent totals of the analytical data with up to 103 wt % (Table 4).

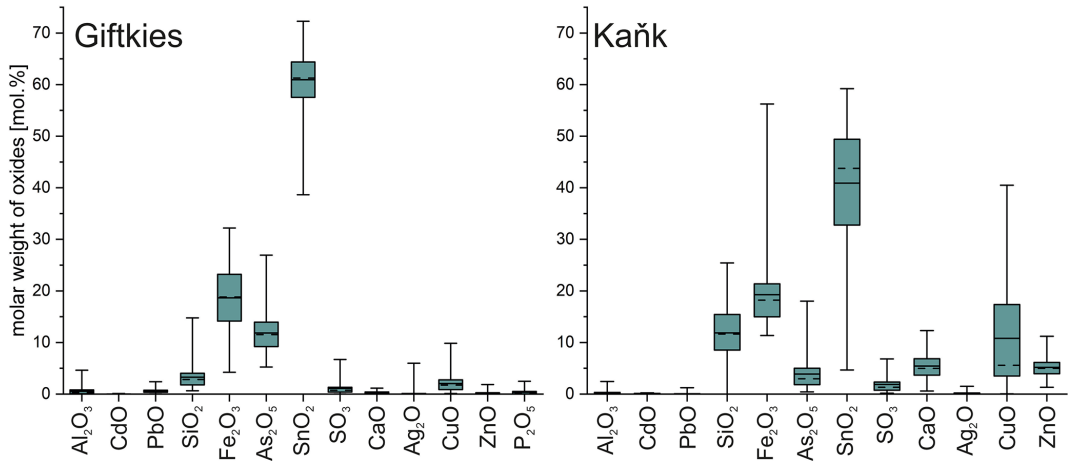

Figure 4. Box plot of the compositional range of SFA precipitates from Giftkies ($n = 221$) and Kaňk ($n = 109$) (average: solid line; median: dashed line; box: 25th–75th percentile; range: minimum–maximum (includes outliers)).

Table 3. WDX analyses of primary sulfides and secondary precipitates observed in the stannite grain from Kaňk (see Fig. 1b). Values are given in percent by weight (wt %; bdl, below detection limit).

	Stannite		Sn-rich chalcopyrite			SFA	Cassiterite	
	1	2	1	2			1	2
Cu	28.88	29.08	26.03	30.08	CuO	5.30	0.30	0.29
Fe	9.37	9.03	25.97	22.80	Fe_2O_3	41.08	1.78	2.23
Zn	6.17	5.87	4.76	5.11	ZnO	0.91	0.07	0.07
As	0.23	0.19	0.08	0.13	As_2O_5	2.34	0.22	0.48
					SiO_2	0.20	bdl	bdl
Sn	25.87	25.81	7.73	6.45	SnO_2	17.33	77.63	76.47
S	29.44	29.44	33.76	33.73	SO_3	0.38	0.18	0.31
Σ	99.96	99.42	98.33	98.30	Σ	93.47	102.35	102.23

4 Discussion

4.1 Primary Sn sulfides

The Sn sulfides of Giftkies and Kaňk have intermediate composition between stannite and ferrokësterite, with highly variable Fe / Zn ratios even within the same locality (Table 1; Figs. 2, 3). Similar variations in Fe and Zn were also reported from the Bleikvassli deposit in Norway, suggesting a non-stoichiometric composition (Cook et al., 1998). In that study, sums of [Fe + Zn] also deviated from the ideal composition, explained by coupled substitution mechanisms with elements on the monovalent (Cu site) or tetravalent (Sn site) position. Such substitution mechanisms were previously reported for the kësterite structure (Zillner et al., 2013; Rios et al., 2016; Bosson et al., 2017) and can also be proposed for stannite.

4.2 Secondary chalcopyrite

Earlier studies described partial miscibility and exsolution features among stannite, chalcopyrite, and sphalerite (Springer, 1968; Nekrasov et al., 1979; Dobrovol'skaya et al., 2008). The miscibility between stannite and chalcopyrite was explained with the substitution of $Sn^{4+} + Fe^{2+}$ for 2 Fe^{3+} (Kase, 1987; Gena et al., 2005) and accounts for the small Sn amounts observed in most chalcopyrite grains (chalcopyrite II) in this study.

However, there exist some chalcopyrite grains which encase stannite and have higher Sn and Zn content (chalcopyrite I) with up to 7.7 wt % and 5.7 wt %, respectively (Fig. 6, Table S1). Two mechanisms are conceivable for the formation of secondary chalcopyrite at studied sites: (i) a diffusion-driven process in the earliest weathering stage or (ii) the dissolution of stannite followed by recrystallization of chalcopyrite. We assume that most of the Sn in stannite was mobilized and transported out of the sulfide by a diffusion-driven process. This results in the transformation of a metastable chalcopyrite solid solution from stannite because of their closely related structures. Copper and Ag are also mobilized from stannite because of their fast self-diffusion (Berger and Bucur, 1996), were reduced at the margins of the sulfide, and precipitated as native metals (Figs. 6–8). The electrons for their reduction were do-

Table 4. WDX analyses of stannite and SFA observed in the weathered stannite grain from Giftkies. Values are given in percent by weight (wt %; nd, not detected).

	Stannite		SFA					
			1	2	3	4	5	6
Cu	28.70	CuO	0.21	0.44	0.47	0.36	0.25	0.16
Ag	nd	AgO	6.75	9.94	0.34	nd	nd	nd
Fe	8.56	Fe_2O_3	13.36	16.59	18.85	17.50	16.52	14.29
Zn	4.59	ZnO	0.03	0.08	0.11	0.08	0.07	0.01
Pb	nd	PbO	1.68	1.42	1.35	1.20	1.29	1.45
As	0.99	As_2O_5	18.65	16.55	17.34	18.93	21.14	19.77
Si	nd	SiO_2	1.37	1.01	0.93	0.91	1.10	2.75
Sn	27.24	SnO_2	53.34	55.97	54.61	53.75	53.12	55.80
S	30.10	SO_3	0.62	0.89	0.39	0.26	0.46	0.32
Σ	100.56	Σ	96.01	102.89	94.39	92.99	93.95	94.55

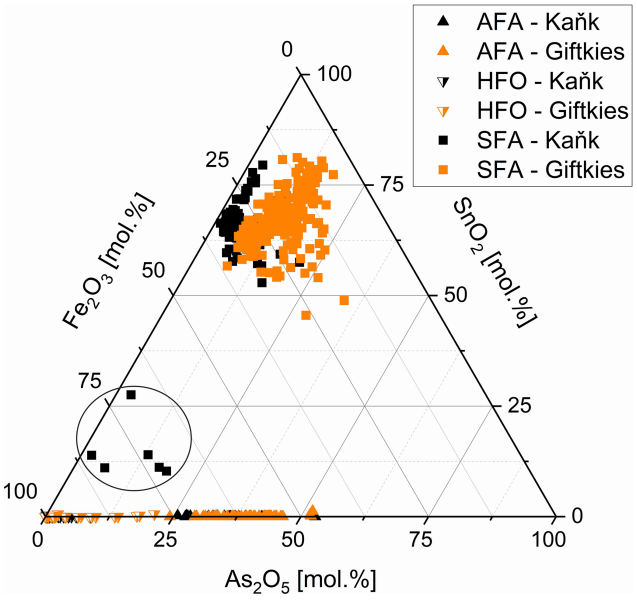

Figure 5. Fe_2O_3, As_2O_5, and SnO_2 abundance in SFA (filled squares), AFA (filled triangles), and HFO (half-filled triangles) from Giftkies (orange) and Kaňk (black); samples within circle are related to chalcopyrite I (all plotted data are normalized to 100 mol %).

nated by the oxidation of sulfur released from the decomposing sulfide material. Iron remains in the sulfide because of its slower self-diffusion than Cu and was enriched in the stannite rim compared to the sulfide core. Zinc also has a fast self-diffusion like Cu (Berger and Bucur, 1996) but remained in part in the solid solution. With time, local enrichments of Zn were formed (Fig. 7) because of the metastable nature of this Sn-rich chalcopyrite. Sphalerite exsolutions are a local co-product (Fig. 6a) of the diffusional process. The residual Sn from the primary stannite is left behind, does not diffuse out, and leads to the formation of a superstructure (Fig. 6b) in the secondary chalcopyrite I.

4.3 Initial weathering: native metals

Sulfides typically decompose in near-surface environments in contact with oxygen and meteoric water. This process was investigated in detail for common sulfides such as arsenopyrite or pyrite (Nickel, 1984; Rimstidt and Vaughan, 2003; Kalin and Harris, 2005; Corkhill and Vaughan, 2009; Drahota and Filippi, 2009; Chandra and Gerson, 2010; Murciego et al., 2011; Romero et al., 2014; Filippi et al., 2015). The decomposition of arsenopyrite and pyrite leads to the release of arsenic, iron, and sulfate and to a pH drop, especially in carbonate-poor environments. It can enhance weathering of other minerals (Nickel, 1984; Filippi et al., 2015). The site Giftkies is carbonate-poor, resulting in pH < 4 in the upper mining waste horizons (Filippi et al., 2015). The waste dumps of Kaňk contain more carbonate than in Giftkies, resulting in a pH of up to 6.5 (Drahota et al., 2018). We assume a deposition under acidic conditions here, which still occurs at several sampling sites at Kaňk (Drahota et al., 2018; Kocourková-Víšková et al., 2015). However, we suppose that the waste dump was mixed with surrounding carbonate-containing soils during the rural landscaping of the area, which increased the pH of the waste dumps.

The initial stages of stannite weathering produced not only the Sn-rich chalcopyrite but also native copper (Figs. 6a, 8a) and native silver (Fig. 8d) in the proximal microenvironments. However, stannite from Giftkies contains only negligible amounts of Ag (Table S1), whereas native silver was observed close to the primary grain surfaces (Fig. 1c). We assume that silver was previously mobilized by the diffusional process or weathering of Ag-bearing stannite. This is indicated by the reprecipitation of native silver between stannite and SFA. It also occurs in close proximity of stannite within the SFA (Fig. 8a), explained by the higher resistance of the

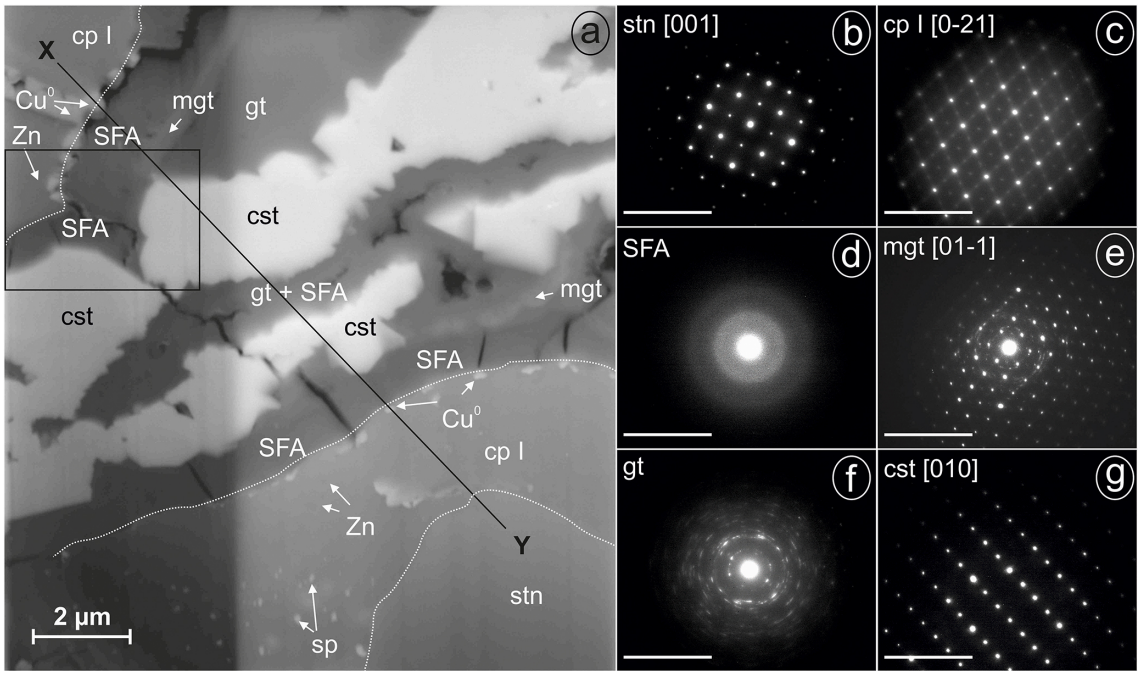

Figure 6. FIB lamella of weathered stannite and SAED patterns of phases (given in reciprocal lattice with $1/10\,\mathrm{nm}^{-1}$ scale) from Kaňk (cp I, Sn-rich chalcopyrite (chalcopyrite I); cst, cassiterite; Cu^0, native copper; gt, goethite; mgt, magnetite; SFA, amorphous Sn–Fe–As phase; sp, sphalerite; stn, stannite; Zn, Zn-rich spots): **(a)** SEM backscattered electron (BSE) image of the lamella with sequences of stannite and secondary precipitates imaged under a tilt angle of 52° (different brightness along the vertical line resulted from the lamella thickness), **(b)** SAED pattern of stannite at point Y in Fig. 6a, **(c)** SAED pattern of chalcopyrite I at point X in Fig. 6a, **(d)** SAED pattern of SFA, **(e)** SAED pattern of magnetite, **(f)** SAED pattern of polycrystalline goethite, and **(g)** SAED pattern of cassiterite.

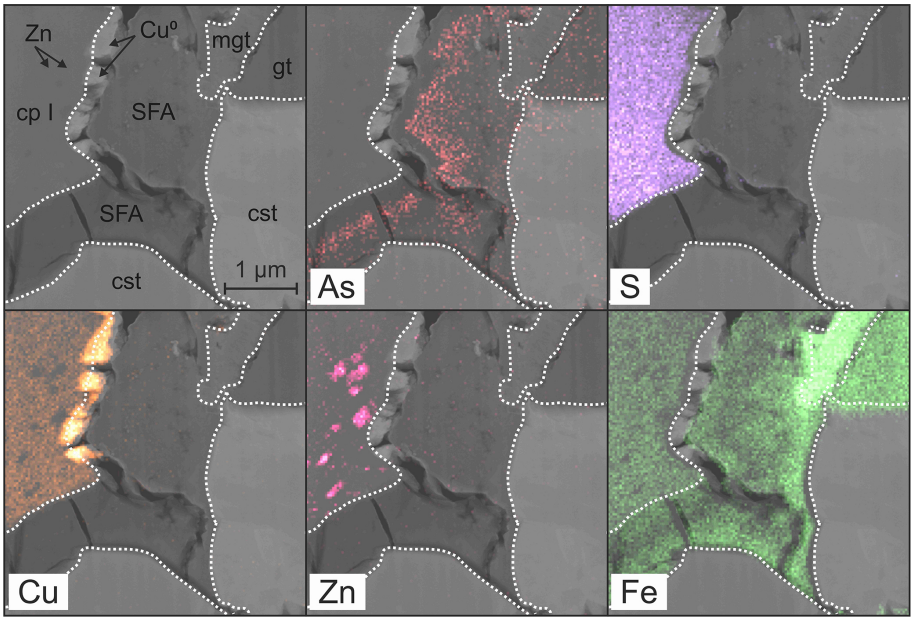

Figure 7. EDX maps of the area indicated in Fig. 6a.

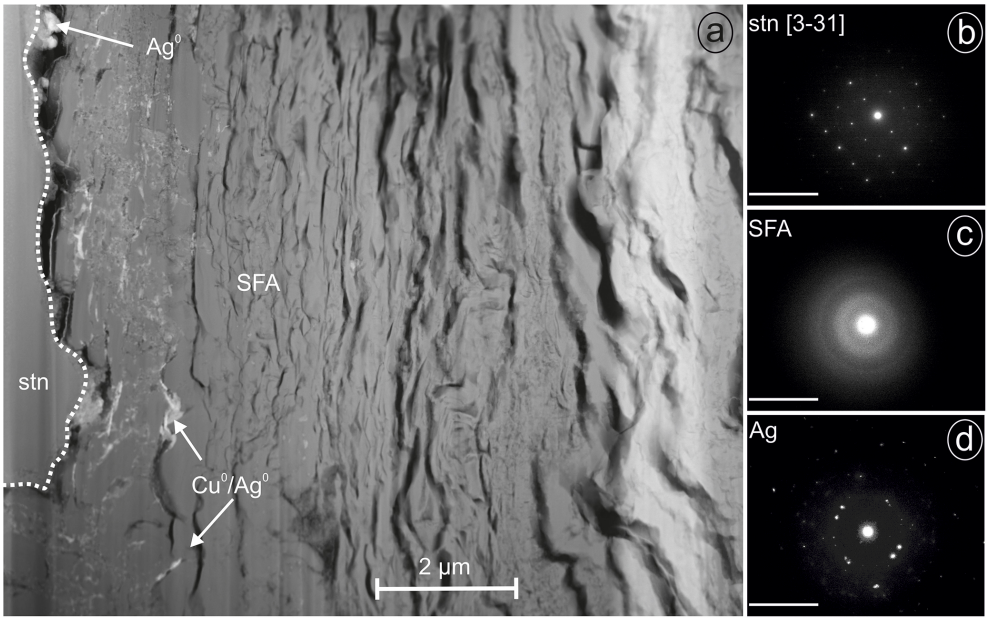

Figure 8. FIB lamella with SAED patterns (given in reciprocal lattice with $1/10\,nm^{-1}$ scale) from Giftkies (Ag^0, native silver; Cu^0, native copper; SFA, amorphous Sn–Fe–As phase; stn, stannite): **(a)** lamella with stannite and a broad band of SFA and native metals, **(b)** SAED pattern of stannite, **(c)** SAED pattern of SFA, and **(d)** SAED pattern of native silver crystals.

native metals to weathering than the sulfides in this environment.

It is known that the elements Cu and Ag have strong affinity to S^{2-} and form secondary sulfides, such as covellite, chalcocite, and acanthite (Nickel, 1984; Majzlan et al., 2018; Bao et al., 2021). The crystallization of native copper and silver in our samples suggests more oxidative conditions than those required for the formation of secondary sulfides. The SFA precipitates in our samples contain only small amounts of sulfur (Fig. 4, Table S3). These observations and analyses suggest that S^{2-} in the primary sulfides is rapidly oxidized and lost, as is also known from other similar sites (Thornber, 1985; Majzlan et al., 2018).

4.4 Initial weathering: SFA precipitates

The SFA precipitated contemporaneously with the formation of the native metals. Chemically, the SFA precipitate is primarily composed of the residual oxides Fe_2O_3 and SnO_2 derived from stannite decomposition but also contains externally added As and Si. The amounts of sequestered Fe_2O_3 and SnO_2 depend on the composition of the primary sulfide as shown for example by Sn-poor and Fe-rich compositions (Fig. 5; Tables S1, S3). The immobile character of Fe^{3+} upon weathering of Fe-rich sulfides results in the precipitation of HFO (Fig. 1d, f; Courtin-Nomade et al., 2003; Moncur et al., 2009). Sequestration of Sn in the amorphous precipitates is the consequence of the limited mobility of Sn (Romero et al., 2014), as also evidenced by the formation of SFA precipitates encrusting stannite (Fig. 1a–c; Filippi et al., 2015; Karwowski and Włodyka, 1981; Kocourková-Víšková et al., 2015). Adsorption of Sn onto HFO is unlikely because of the limited mobility of Sn and its cationic nature over a wide pH range (Haase et al., 2021). This is supported by the high Sn content of the precipitates compared to their Fe content, which excludes the adsorption of all the Sn onto HFO because of its limited sorption sites.

Arsenic is a major component of the SFA precipitate, and the As enrichment was driven by its release from the primary arsenopyrite. In the absence of Sn sulfides, the dissolution of arsenopyrite results in the formation of crystalline arsenates and AFA under acidic conditions (Paktunc et al., 2008; Drahota and Filippi, 2009). Scorodite is the most common product, but AFA can also precipitate as a secondary arsenate (Drahota and Filippi, 2009; Filippi et al., 2015; Kocourková-Víšková et al., 2015). AFA is metastable and transforms into scorodite at low pH (Drahota and Filippi, 2009). Scorodite dissolves incongruently (Krause and Ettel, 1989; Paktunc et al., 2008; Drahota and Filippi, 2009; Murciego et al., 2011) with decreasing time and rising pH (Harvey et al., 2006) resulting in the precipitation of HFO and the release of arsenate species (Drahota and Filippi, 2009). Under acidic conditions, HFO and SFA precipitates are able to take up arsenate from solution. Little is known about the incorporation mechanism of As_2O_5 in SFA, but its uptake capacity is large (Figs. 4, 5). Such a scavenging behaviour is also known from HFO, which can take up to 21.7 wt % As_2O_5 (Murciego et al., 2011). Arsenic then stabilizes the precipitate and retards the transformation of HFO to stable products (Ford, 2002) as could be also assumed for SFA. Romero et al. (2014) re-

ported similar SFA precipitates to those found in our work. Those authors assumed that those precipitates consisted of Fe-rich cassiterite and arsenic was adsorbed on their surface. Our TEM results refute such a possibility for the material studied here.

4.5 Initial weathering: adsorption on secondary precipitates

The SFA precipitate contains small amounts of other oxide components (Fig. 4), which are presumably adsorbed on the surface of the particles. The nature and capacity of adsorption mainly depend on the pH, point of zero charge (PZC) of the adsorbent, aqueous nature of the adsorbates, and the availability and competition of ions and molecules for adsorption sites (Gadde and Laitinen, 1974; Kosmulski, 2009a, b). The pH ranges from 3.3–5.8 and 2.4–6.5 for Giftkies and Kaňk, respectively (Drahota et al., 2018; Filippi et al., 2015; Kocourková-Víšková et al., 2015), whereas the PZC of SnO_2 and hydrous stannates is 3.9–5.5 (Kosmulski, 2009b). Ghoneimy et al. (1997) investigated the PZC of synthetic hydrous stannic oxide, mixed hydrous ferric / stannic oxide, and HFO and obtained a PZC of 4.4, 6.2, and 6.8, respectively. This suggests a lower PZC of Sn-containing Fe precipitates, and a PZC of SFA was assumed to be in the range of PZC_{SnO_2} and PZC_{HFO} at studied sites.

The assumed PZC for SFA within the range 4–7 indicates a preferred adsorption of anionic species (e.g. AsO_4^{3-}, PO_4^{3-}) and dissolution of cationic species under acidic conditions. The elements Pb, Cu, Zn, and Cd prevail as cations under such conditions and are retained in small amounts in the secondary precipitates derived from the decomposition of galena (Nickel, 1984; Thornber, 1985; Filippi et al., 2015; Bao et al., 2021) and stannite. Previous studies have shown a decreased mobility for these elements at pH > 4 because of adsorption on HFO (Drahota et al., 2018; Gadde and Laitinen, 1974; Nickel, 1984; Moncur et al., 2009; Tiberg et al., 2013) or incorporation in secondary precipitates, e.g. Pb in jarosite (Drahota et al., 2018).

The oxide components CaO, SiO_2, Al_2O_3, and P_2O_5 in SFA are primarily derived from acid-soluble silicates and phosphates such as feldspars and apatite, respectively (Nickel, 1984; Welch and Ullman, 1996; Nugent et al., 1998; Guidry and Mackenzie, 2000; Harris, 2002; Murciego et al., 2011). Under acidic conditions, feldspars (especially plagioclase) and apatite decompose and release ions (Ca^{2+}, Al^{3+}, PO_4^{3-}) and neutral species ($H_4SiO_4^0$) to the solution. Scavenging phases such as HFO and SFA take up the ions and molecules via adsorption or polymerization on the surface (Thornber, 1985; Schaller et al., 2020).

4.6 Enhanced weathering

As the weathering advances, crystalline Fe and Sn minerals such as goethite and cassiterite appear in the samples. The spatial relationship among the weathering products indicates that the crystalline phases formed by recrystallization of the amorphous precipitate. The occurrence of the spinel with acicular morphology is more difficult to explain. Assuming that this spinel is magnetite, it could have been formed due to the oxidation of S^{2-} coupled with the reduction of Fe^{3+} to Fe^{2+} (Rimstidt and Vaughan, 2003). The acicular morphology could have been acquired by the solid-state transformation of acicular goethite under such redox conditions (Usman et al., 2013). Especially poorly crystalline goethite with a large surface area could be prone to such transformations (Usman et al., 2013). The second possibility is the pseudomorph replacement of hematite by magnetite under reducing conditions (mushketovitization). However, no hematite remnants were found in the weathering zones of the Sn sulfide. Therefore, we favour the formation of spinel from goethite over the mushketovitization in this study. Another possibility is pseudomorphs of magnetite after green rust. Such phases are transient, reactive minerals found in environments with abundant Fe^{3+} and Fe^{2+}. Their platy crystals, if cut perpendicularly to the basal faces, could be responsible for the observed acicular morphology. With increasing O_2 concentration, green rust transforms to magnetite under the release of water under slightly alkaline conditions (Schwertmann and Cornell, 1991). At the sites studied, however, the conditions are acidic, and therefore the solid-state transformation from goethite seems to be a more likely pathway for magnetite production.

The metastable HFO and the Fe_2O_3 component in SFA transform with time into stable goethite. This transformation is accompanied by a reduction in the specific surface area (Schwertmann and Cornell, 1991) and release of the adsorbed ions (Courtin-Nomade et al., 2003; Paktunc et al., 2008). Our TEM–EDX data show that the resulting goethite still retains small amounts of As.

The absence of Sn in goethite confirms the remobilization of Sn during the transformation. The released Sn is deposited in the secondary cassiterite (Balboni et al., 2020), as the ultimate sink of Sn, the most common and stable Sn mineral at the Earth's surface (Lottermoser and Ashley, 2006; Rai et al., 2011). The resistance of cassiterite to weathering was also observed from oxide zones of supergene deposits (Nickel, 1984) and supports the findings of this study. There must be, however, conditions under which Sn is transferred into aqueous solutions that become supersaturated with respect to cassiterite (Haase et al., 2021). Such conditions, especially strongly acidic environments, could be generated in environments rich in massive sulfides, especially pyrite.

5 Conclusions

Tin minerals of the stannite–kësterite series decompose under oxidative conditions in a complex assemblage of secondary minerals. In the initial stages of weathering, native

copper and silver were formed at Kaňk and Giftkies, respectively. Amorphous and metastable Sn precipitates cover the stannite and witness very limited mobility of Sn into oxygen- and water-rich environments. The precipitate is Fe- and Sn-rich and takes up high amounts of As derived from arsenopyrite decomposition. With ageing, magnetite, goethite, and cassiterite crystallize from the amorphous or poorly crystalline precursor and mark the end of the weathering cycle of stannite by these stable minerals. Other elements derived from stannite become mobilized in the initial stage of weathering (e.g. Zn, S) or after full oxidation of the sulfidic material in the weathering zone (e.g. Cu, Ag).

Data availability. Data sets used in this paper are available upon request.

Supplement. The supplement related to this article is available online at: https://doi.org/10.5194/ejm-34-493-2022-supplement.

Author contributions. PH, PD, and JM collected samples. PH and SK performed EMP analysis. PH and KP performed FIB–SEM and TEM analysis. PH wrote the paper, and all authors revised the manuscript.

Competing interests. The contact author has declared that none of the authors has any competing interests.

Disclaimer. Publisher's note: Copernicus Publications remains neutral with regard to jurisdictional claims in published maps and institutional affiliations.

Acknowledgements. We thank the reviewers Stefano Naitza and Pierfranco Lattanzi, who helped to improve the manuscript.

Financial support. This research has been supported by the Deutsche Forschungsgemeinschaft (grant nos. MA 3927/35-1 and LA 830/14-1).

Review statement. This paper was edited by Giovanni De Giudici and reviewed by Pierfranco Lattanzi and Stefano Naitza.

References

Abraitis, P. K., Pattrick, R. A. D., and Vaughan, D. J.: Variations in the compositional, textural and electrical properties of natural pyrite: a review, Int. J. Miner. Process., 74, 41–59, https://doi.org/10.1016/j.minpro.2003.09.002, 2004.

Balboni, E., Smith, K. F., Moreau, L. M., Li, T. T., Maloubier, M., Booth, C. H., Kersting, A. B., and Zavarin, M.: Transformation of ferrihydrite to goethite and the fate of plutonium, ACS Earth Space Chem., 4, 1993–2006, https://doi.org/10.1021/acsearthspacechem.0c00195, 2020.

Bao, Z., Al, T., Couillard, M., Poirier, G., Bain, J., Shrimpton, H.K., Finfrock, Y. Z., Lanzirotti, A., Paktunc, D., Saurette, E., Hu, Y., Ptacek, C. J., and Blowes, D. W.: A cross scale investigation of galena oxidation and controls on mobilization of lead in mine waste rock, J. Hazard. Mater., 412, 125130, https://doi.org/10.1016/j.jhazmat.2021.125130, 2021.

Berger, R. and Bucur, R. V.: Diffusion in copper sulphides – an experimental study of chalcocite, chalcopyrite and bornite, Report to the Swedish Nuclear Power Inpsectorate, Uppsala University Sweden, 36 pp., SKI-R-96-3, ISSN 1104-1374, 1996.

Bosson, C. J., Birch, M. T., Halliday, D. P., Tang, C. C., Kleppe, A. K., and Hatton, P. D.: Polymorphism in Cu_2ZnSnS_4 and new off-stoichiometric crystal structure types, Chem. Mater., 29, 9829–9839, https://doi.org/10.1021/acs.chemmater.7b04010, 2017.

Caye, R., Laurent, Y., Picot, P., and Pierrot, R.: La hocartite, Ag_2SnFeS_4, une novelle espèce minérale, B. Mineral., 91, 383–387, 1968.

Černý, P., Masau, M., Ercit, T. S., Chapman, R., and Chackowsky, L.E.: Stannite and këwhile from the Peerless pegmatite, Black Hills, South Dakota, USA, J. Geosci-Czech., 46, 27–33, 2001.

Chandra A. P. and Gerson, A. R.: The mechanisms of pyrite oxidation and leaching: A fundamental perspective, Surf. Sci. Rep., 65, 293–315, https://doi.org/10.1016/j.surfrep.2010.08.003, 2010.

Chen, S.-C., Yu, J.-J., Bi, M.-F., and Lehmann, B.: Tin-bearing minerals at the Furong tin deposit, South China: Implications for tin mineralization, Chem. Erde-Geochem., 82, 125856, https://doi.org/10.1016/j.chemer.2021.125856, 2022.

Coleman, L. C.: Mineralogy of the Yellowknife Bay Area, N.W.T., Am. Mineral., 38, 506–527, 1953.

Cook, N. J., Spry, P. G., and Vokes, F. M.: Mineralogy and textural relationships among sulphosalts and related minerals in the Bleikvassli Zn-Pb-(Cu) deposit, Nordland, Norway, Miner. Deposita., 34, 35–56, https://doi.org/10.1007/s001260050184, 1998.

Corkhill, C. I. and Vaughan, D. J.: Arsenopyrite oxidation – A review, Appl. Geochem., 24, 2342–2361, https://doi.org/10.1016/j.apgeochem.2009.09.008, 2009.

Courtin-Nomade, A., Bril, H., Neel, C., and Lenain, J.-F.: Arsenic in iron cements developed within tailings of a former metalliferous mine – Enguialès, Aveyron, France, Appl. Geochem., 18, 395–408, https://doi.org/10.1016/S0883-2927(02)00098-7, 2003.

Courtin-Nomade, A., Bril, H., Bény, J.-M., Kunz, M., and Tamura, N.: Sulfide oxidation observed using micro-Raman spectroscopy and micro-X-ray diffraction: The importance of water / rock ratios and pH conditions, Am. Mineral., 95, 582–591, https://doi.org/10.2138/am.2010.3331, 2010.

Dobrovol'skaya, M. G., Genkin, A. D., Bortnikov, N. S., and Golovanova, T. I.: Unusual sphalerite, chalcopyrite, and stannite intergrowths at tin deposits, Geol. Ore Deposits, 50, 75–85, https://doi.org/10.1134/S1075701508010042, 2008.

Drahota, P. and Filippi, M.: Secondary arsenic minerals in the environment: A review, Environ. Int., 35, 1243–1255, https://doi.org/10.1016/j.envint.2009.07.004, 2009.

Drahota, P., Raus, K., Rychlíková, E., and Rohovec, J.: Bioaccessibility of As, Cu, Pb, and Zn in mine waste, urban soil, and road dust in the historical mining village of Kaňk, Czech Republic, Environ. Geochem. Health, 40, 1495–1512, https://doi.org/10.1007/s10653-017-9999-1, 2018.

Durant, B. K. and Parkinson, B. A.: Photovoltaic response of natural Kesterite crystals, Sol. Energ. Mat. Sol. C., 144, 586–591, https://doi.org/10.1016/j.solmat.2015.09.055, 2016.

Ettler, V., Sejkora, J., Drahota, P., Litochleb, J., Pauliš, P., Zeman, J., Novák, M., and Pašava J.: Příbram and Kutná Hora mining districts – from historical mining to recent environmental impact, IMA 2010, Budapest, Acta Mineral.-Petrogr. Field Guide Ser., 7, 1–23, 2010.

Eugster, H. P.: Granites and hydrothermal ore deposits: a geochemical framework, Mineral. Mag., 49, 7–23, https://doi.org/10.1180/minmag.1985.049.350.02, 1984.

Filippi, M., Drahota, P., Machovič, V., Böhmová, V., and Mihaljevič, M.: Arsenic mineralogy and mobility in the arsenic-rich historical mine waste dump, Sci. Total Environ., 536, 713–728, https://doi.org/10.1016/j.scitotenv.2015.07.113, 2015.

Ford, R.: Rates of hydrous ferric oxide crystallization and the influence on coprecipitated arsenate, Environ. Sci. Technol., 36, 2459–2463, https://doi.org/10.1021/es015768d, 2002.

Gadde, R. R. and Laitinen, H. A.: Studies of heavy metal adsorption by hydrous iron and manganese oxides, Anal. Chem., 46, 2022–2026, https://doi.org/10.1021/ac60349a004, 1974.

Gena, K., Chiba, H., and Kase, K.: Tin-bearing chalcopyrite and platinum-bearing bismuthinite in the active Tiger chimney, Yonaguni Knoll IV seafloor hydrothermal system, South Okinawa Trough, Japan, Okayama Univ. Earth Sci. Rep., 12, 1–5, doi.org/10.18926/ESR/13850, 2005.

Ghoneimy, H. F., Morcos, T. N., and Misak, N. Z.: Adsorption of Co^{2+} and Zn^{2+} ions on hydrous Fe(III), Sn(IV) and mixed Fe(III) / Sn(IV) oxides, Part I. Characteristics of the hydrous oxides, apparent capacity and some equilibria measurements, Colloid. Surface. A, 122, 13–26, https://doi.org/10.1016/S0927-7757(96)03854-X, 1997.

Guidry, M. W. and Mackenzie, F. T.: Apatite weathering and the Phanerozoic phosphorous cycle, Geology, 28, 631–634, https://doi.org/10.1130/0091-7613(2000)28<631:AWATPP>2.0.CO;2, 2000.

Haase, P., Christensen, H. G., Nielsen, U. G., Koch, C. B., Galazka, Z., and Majzlan, J.: Stability and solubility of members of tin perovskites in the schoenfliesite subgroup, $\square_2(BSn^{4+})(OH,O)_6$(B = Ca, Fe^{3+}, Mg, Mn^{2+}, Zn, Cu), Chem. Thermodyn. Therm. Anal., 1/2, 100005, doi.org/10.1016/j.ctta.2021.100005, 2021.

Harris, W. G.: Phosphate minerals, in: Soil mineralogy with environmental applications, edited by: Dixon, J. B. and Schulze, D. G., SSSA book series 7, Madison, USA, Soil Sci. Soc. Am., 637–665, ISBN 0891188398, 2002.

Harvey, M. C., Schreiber, M. E., Rimstidt, J. D., and Griffith, M. M.: Scorodite dissolution kinetics: Implications for arsenic release, Envrion. Sci. Technol., 40, 6709–6714, https://doi.org/10.1021/es061399f, 2006.

Jambor, J. L. and Dutrizac, J. E.: Occurrence and constitution of natural and synthetic ferrihydrite, a widespread iron oxyhydroxide, Chem. Rev., 98, 2549–2585, https://doi.org/10.1021/cr970105t, 1998.

Johan, Z. and Picot, P.: La pirquitasite Ag_2ZnSnS_4, un nouveau member du groupe de la stannite, B. Mineral., 105, 229–235, 1982.

Kalin, M. and Harris, B.: Chemical precipitation within pyritic waste rock, Hydrometallurgy, 78, 209-225, https://doi.org/10.1016/j.hydromet.2005.03.008, 2005.

Karwowski, Ł. and Włodyka, R.: Stannite in the cassiterite-sulfide deposits of the Izera Mts (Sudetes), Acta Geol. Pol., 31, 41–47, 1981.

Kase, K.: Tin-bearing chalcopyrite from the Izumo vein, Toyoha mine, Hokkaido, Japan, Can. Mineral., 25, 9–13, 1987.

Kissin, S. A., Owens, D. R., and Roberts, W. L.: Černýite, a copper-cadmium-tin sulfide with the stannite structure, Can. Mineral., 16, 139–146, 1978.

Kocourková-Víšková, E., Loun, J., and Sracek, O.: Secondary arsenic minerals and arsenic mobility in a historical waste rock pile at Kaňk near Kutná Hora, Czech Republic, Miner. Petrol., 109, 17–33, https://doi.org/10.1007/s00710-014-0356-0, 2015.

Kosmulski, M.: Surface charging and points of zero charge, CRC Press, Boca Raton, Florida, USA, 1092 p., Taylor & Francis Group, https://doi.org/10.1201/9781420051896, 2009a.

Kosmulski, M.: Compilation of PZC and IEP of sparingly soluble metal oxides and hydroxides from literature, Adv. Colloid Interfac., 152, 14–25, https://doi.org/10.1016/j.cis.2009.08.003, 2009b.

Krause, E. and Ettel, V. A.: Solubilities and stabilities of ferric arsenate compounds, Hydrometallurgy, 22, 311–337, https://doi.org/10.1016/0304-386X(89)90028-5, 1989.

Landes, K. K.: Sequence of mineralization in the Keystone, South Dakota, pegmatites, Am. Mineral., 13, 537–558, 1928.

Lottermoser, B. G. and Ashley, P. M.: Mobility and retention of trace elements in hardpan-cemented cassiterite tailings, North Queensland, Australia, Environ. Geol., 50, 835–846, https://doi.org/10.1007/s00254-006-0255-8, 2006.

Majzlan, J., Kiefer, S., Herrmann, J., Števko, M., Sejkora, J., Chovan, M., Lánczos, T., Lazarov, M., Gerdes, A., Langenhorst, F., Radková, A. B., Jamieson, H., and Milovský, R.: Synergies in elemental mobility during weathering of tetrahedrite $[(Cu,Fe,Zn)_{12}(Sb,As)_4S_{13}]$: Field observations, electron microscopy, isotopes of Cu, C, O, radiometric dating, and water geochemistry, Chem. Geol., 488, 1–20, https://doi.org/10.1016/j.chemgeo.2018.04.021, 2018.

Moncur, M. C., Jambor, J. L., Ptacek, C. J., and Blowes, D. W.: Mine drainage from the weathering of sulfide minerals and magnetite, Appl. Geochem., 24, 2362–2373, https://doi.org/10.1016/j.apgeochem.2009.09.013, 2009.

Müller, B.: Some aspects of the geochemistry of tin in hydrothermal solutions, Doctoral Thesis, ETH Zürich, Switzerland, 96 pp., https://doi.org/10.3929/ethz-a-003877734, 1999.

Murciego, A., Álvarez-Ayuso, E., Pellitero, E., Rodriguez, M. A., García-Sánchez, A., Tamayo, A., Rubio, J., Rubio, F., and Jubin, J.: Study of arsenopyrite weathering products in mine wastes from abandoned tungsten and tin exploitations, J. Hazard. Mater., 186, 590–601, https://doi.org/10.1016/j.jhazmat.2010.11.033, 2011.

Neiva, A. M. R.: Geochemistry of tin-bearing granitic rocks, Chem. Geol., 43, 241–256, https://doi.org/10.1016/0009-2541(84)90052-4, 1984.

Nekrasov, I. J., Sorokin, V. I., and Osadchii, E. G.: Fe and Zn partitioning between stannite and sphalerite and its application in geothermometry, Phys. Chem. Earth, 11, 739–742, https://doi.org/10.1016/0079-1946(79)90069-7, 1979.

Nickel, E. H.: The mineralogy and geochemistry of the weathering profile of the Teutonic Bore Cu-Pb-Zn-Ag sulphide deposit, J. Geochem. Explor., 22, 239–264, https://doi.org/10.1016/0375-6742(84)90014-1, 1984.

Nugent, M. A., Brantley, S. L., Pantano, C. G., and Maurice, P. A.: The influence of natural mineral coatings on feldspar weathering, Nature, 396, 527–622, https://doi.org/10.1038/26951, 1998.

Ondruš, P., Veselovský, F., Gabašová, A., Drábek, M., Dobeš, P., Malý, K., Hloušek, J., and Sejkora, J.: Ore-forming processes and mineral paragenesis of the Jáchymov ore district, J. Geosci-Czech., 48, 157–192, 2003.

Paktunc, D., Dutrizac, J., and Gertsman, V.: Synthesis and phase transformations involving scorodite, ferric arsenate and arsenical ferrihydrite: Implications for arsenic mobility, Geochim. Cosmochim. Ac., 72, 2649–2672, https://doi.org/10.1016/j.gca.2008.03.012, 2008.

Rai, D., Yui, M., and Schaef, H. T.: Thermodynamic model for SnO_2(cr) and SnO_2(am) solubility in the aqueous Na^+-H^+-OH–Cl–H_2O system, J. Solution Chem., 40, 1155, https://doi.org/10.1007/s10953-011-9723-1, 2011.

Rimstidt, J. D. and Vaughan, D. J.: Pyrite oxidation: A state-of-the-art assessment of the reaction mechanism, Geochim. Cosmochim. Ac., 67, 873–880, https://doi.org/10.1016/S0016-7037(02)01165-1, 2003.

Rios, L. E. V., Neldner, K., Gurieva, G., and Schorr, S.: Existence of off-stoichiometric single phase këserite, J. Alloy Compd., 657, 408–413, https://doi.org/10.1016/j.jallcom.2015.09.198, 2016.

Romero, F. M., Canet, C., Alfonso, P., Zambrana, R. N., and Soto, N.: The role of cassiterite controlling arsenic mobility in an abandoned stanniferous tailings impoundment at Llallagua, Bolivia, Sci. Total Environ., 481, 100–107, https://doi.org/10.1016/j.scitotenv.2014.02.002, 2014.

Schaller, J., Frei, S., Rohn, L., and Gilfedder, B.S.: Amorphous silica controls water storage capacity and phosphorous mobility in soils, Front. Environ. Sci., 8, 94, 12 pp., https://doi.org/10.3389/fenvs.2020.00094, 2020.

Schmidt, C.: Formation of hydrothermal tin deposits: Raman spectroscopic evidence for an important role of aqueous Sn(IV) species, Geochim. Cosmochim. Ac., 220, 499–511, https://doi.org/10.1016/j.gca.2017.10.011, 2018.

Schwertmann, U. and Cornell, R. M.: Iron oxides in the laboratory – preparation and characterization, Wiley-VCH Verlag, Weinheim, Germany, VCH, ISBN 3-527-26991-6, 1991.

Smeds, S.-A.: Trace elements in in potassium-feldspar and muscovite as a guide in the prospecting for lithium- and tin-bearing pegmatites in Sweden, J. Geochem. Explor., 42, 351–369, https://doi.org/10.1016/0375-6742(92)90032-4, 1992.

Springer, G.: Electronprobe analyses of stannite and related tin minerals, Mineral. Mag., 36, 1045–1051, https://doi.org/10.1180/minmag.1968.036.284.02, 1968.

Thornber, M. R.: Supergene alteration of sulphides, VII. Distribution of elements during the gossan-forming process, Chem. Geol., 53, 279–301, https://doi.org/10.1016/0009-2541(85)90075-0, 1985.

Tiberg, C., Sjöstedt, C., Persson, I., and Gustafsson, J. P.: Phosphate effects on copper(II) and lead(II) sorption to ferrihydrite, Geochim. Cosmochim. Ac., 120, 140–157, https://doi.org/10.1016/j.gca.2013.06.012, 2013.

Usman, M., Abdelmoula, M., Faure, P., Ruby, C., and Hanna, K.: Transformation of various kinds of goethite into magnetite: Effect of chemical and surface properties, Geoderma, 197/198, 9–16, https://doi.org/10.1016/j.geoderma.2012.12.015, 2013.

Welch, S. A. and Ullman, W. J.: Feldspar dissolution in acidic and organic solutions: Compositional and pH dependence of dissolution rate, Geochim. Cosmochim. Ac., 60, 2939–2948, https://doi.org/10.1016/0016-7037(96)00134-2, 1996.

Zillner, E., Paul, A., Jutimoosik, J., Chandarak, S., Monnor, T., Rujirawat, S., Yimnirum, R., Lin, X. Z., Ennaoui, A., Dittrich, T., and Lux-Steiner, M.: Lattice positions of Sn in Cu_2ZnSnS_4 nanoparticles and thin films studied by synchrotron X-ray absorption near edge structure analysis, Appl. Phys. Lett., 102, 221908, https://doi.org/10.1063/1.4809824, 2013.